Efficient dual-scale flow simulation for Resin Transfer Molding process based on domains skeletonization

Simone Bancora, Christophe Binetruy, Suresh Advani, Sebastien Comas-Cardona, Adrien Leygue

Efficient dual-scale flow simulation for Resin Transfer Molding process based on domains skeletonization

S. Bancora[a], C. Binetruy[a,b,*], S. Advani[b,a], S. Comas-Cardona[a], A. Leygue[a]

[a] *Nantes Université, École Centrale Nantes, CNRS, GeM, UMR 6183, F-44000, France*
[b] *Center for Composite Materials, University of Delaware, Newark, Delaware 19716, USA*

Abstract

In the Resin Transfer Molding (RTM) process, a polymeric resin is injected inside a dry preform to fill the gaps around and inside the fiber tows. Simulating this process at the scale of the tows is challenging because of the computational cost associated to solving a three-dimensional dual-scale flow problem. In this work, a novel Dual-Scale Skeleton model (DSS) is introduced, capable of solving a dual-scale flow problem at an affordable computational cost. The three-dimensional geometry of a multi-layer layup, consisting of inter-tow channels and permeable tows, is replaced by a skeletonized representation of the original subdomains. Dual-scale flow is modeled using a Reynolds-Darcy finite elements formulation. The model is validated numerically and its application is demonstrated over a few test cases. The adoption of the DSS model allows one to simulate complex dual-scale flow problems over large domains at a reduced computational cost when compared to full 3D solutions.

Keywords: C. Process Modeling, C. Finite element analysis (FEA), E. Resin transfer moulding (RTM), Skeletonization

*Corresponding author
Email address: christophe.binetruy@ec-nantes.fr (C. Binetruy)

1. Introduction

Resin Transfer Moulding (RTM) is a family of Liquid Composite Moulding (LCM) processes used to produce net shape composite structural parts in which a fibrous preform is compressed inside a rigid mould and impregnated with a thermoset resin. After the resin cures, the solidified part is demoulded [1]. When manufacturing parts using the RTM process, engineers are interested in predicting the filling pattern to ensure no defects such as dry preform regions or voids will occur due to insufficient infiltration. This is typically explored using numerical simulations to model the macroscopic flow inside the fibrous material using Darcy's law [2, 3]. Such simulations can also be used to design and introduce flow control in the process to prevent defects [4, 5] However, simulations rely on assigning the preform permeability values that quantify the resistance of the microstructure to resin flow. This upscaled tensorial quantity can be estimated by experimental characterization on a flat sample material [6, 7], or can be analytically or numerically characterized [8]. In recent years, significant efforts have been devoted to the numerical characterization of permeability. By simulating Stokes flow at the mesoscale inside a digital Representative Volume Element (RVE) of the material [9, 10, 11], the pressure drop in the domain can be measured and the macroscale permeability tensor of the sample can be calculated. However, the high computational cost associated with the simulation of a 3D dual-scale flow limits the size of the domain to a few centimeters and is not representative of the complex preform microstructure [12]. As of today, 3D mesoscale simulations allow one to estimate the permeability of a material but simulating the filling of an entire part at that scale is unfeasible and cannot be used to optimize the process[13]. Due to this limitation, long range features (local defects, ply drop-offs, change in fiber orientations) and their effect on the filling process cannot be taken into account. In the attempt to expand the domain size, researchers look at alternatives to solving a full Stokes flow and reduce the computational cost of

the problem. Examples applied to textiles are the Pore Network Model (PNM) [14] or the Lattice-Boltzmann method (LBM) [15], with the advantage of a lower number of unknowns to be resolved than the number of DOFs required by a detailed mesh. In the present work, the approach known as skeletonization is explored: the topological *medial skeleton* of a three-dimensional geometry is extracted, and then the flow problem is solved on a new two-dimensional space at a reduced computational cost.

Skeleton-based models. Medial skeletons of shapes were historically introduced by Blum in 1967, defined as the "locus of centers of maximal spheres bi-tangent to the shape boundaries" [16]. The geometrical nature of the skeleton is dependent on the topological dimension of the original geometry: the medial skeleton of a three-dimensional set of boundary surfaces is built as a set of surfaces described by the points equidistant from the boundaries. In its numerical form, such geometrical object is discretized as a surface mesh of two-dimensional elements. Today a number of numerical algorithms have been developed for the extraction of medial skeletons from complex shapes, such as the Voronoi method [17, 18], the Grassfire method [19], the sequential Betti-number based algorithm [20], the extended shrinking algorithm [21], and distance-transform (DT) based algorithms [22]. A comprehensive review of skeletonization algorithms was realised by Saha et al. [23].

Casting a three-dimensional problem onto a two-dimensional space requires making some assumptions about the governing equations. Typically, for the case of creeping flow inside narrow gaps, lubrication theory is used [24]. The transverse velocity of the fluid is neglected and the local gap height is captured in the hydraulic permeability term $h^2/12$ contained in the Reynolds equation. Lubrication has been historically employed to model flow in bearings [25] and in porous rocks containing a network of fractures [26, 27, 28]. Flow models in porous media based on medial skeletons and lubrication have been developed before, for example in [29, 30, 31]. Random

porous media structures were reduced to skeleton representations using Voronoi diagram method [32]. Wong et al. [11] solved lubricated flow on a 1D medial axis mesh to compute the upscaled permeability of textiles. They anticipated the possibility to extend the approach to three-dimensional space, proposing to solve a lubricated flow problem on a "stream surface" mesh. In [33] lubricated flow on the Medial Surface skeleton mesh was tested against full-dimensional Stokes flow for several test cases, including calculating the permeability of selected textiles. To the best of the authors' knowledge, all of the skeleton-based models proposed so far are based on single-scale flow. Defining a medial skeleton for a dual-scale domain is challenging since adjacent subdomains are reduced to non-connected skeletons. Formulating a dual-scale flow model based on skeleton domains requires a new definition of a dual-scale skeleton.

Objective. In this work a novel Dual Scale Skeleton (DSS) model is introduced: a skeleton-based model to address dual-scale flow typically encountered in RTM processes. First, a new definition of dual-scale skeleton domain is presented. Then the DSS model is formulated and validated by comparison with a full-dimensional solution. Finally, a series of filling simulation test cases are presented to showcase the potential of the model for next generation RTM process simulations.

2. Methodology

2.1. Medial Skeleton mesh

The classical definition of a medial skeleton mesh, which is limited to single domain geometries, needs to be adapted for dual-scale flow models. When adjacent subdomains in a dual-scale input geometry (channels and yarns) are reduced to their skeleton form, their physical connection at the interface is lost because two separate skeleton subdomains are obtained. To address the interaction between channels and yarns, some form of connectivity must be reintroduced between these separated skeletons. A modified

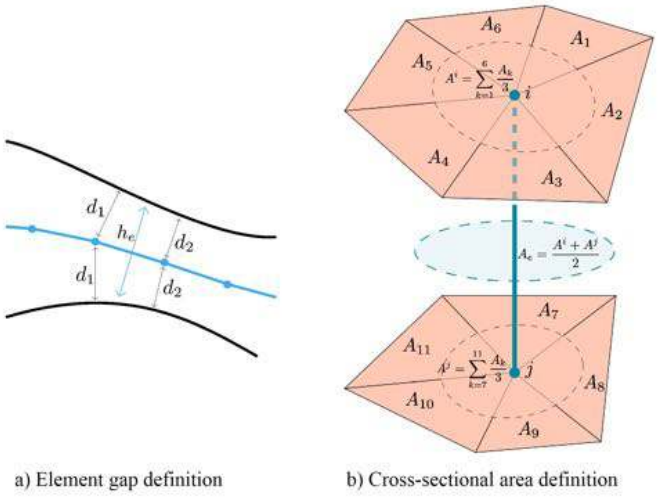

Figure 1: Illustrated definition of geometrical quantities in the hybrid skeleton mesh; a) element size, 2D example; b) definition of cross-section area assigned to 1D elements

definition of medial skeleton mesh is proposed, named *hybrid skeleton mesh*: channels and yarns are generated as independent skeleton meshes, and then assembled into one global skeleton mesh by addition of interface elements. The hybrid skeleton mesh can be obtained from any 3D elements mesh which presents at least two separate volume subdomains. These correspond to the channels and the yarns subdomain, which will be referred to as Ω_1 (channels) and Ω_2 (yarns) respectively. An example of input mesh is shown in Fig. 2a, which represents a porous yarn immersed in a channel. Subdomains Ω_1 and Ω_2 are reduced to their skeleton meshes $\hat{\Omega}_1$ and $\hat{\Omega}_2$ respectively (triangular elements). At every vertex i the distance d_i between the node and the input geometry boundary is calculated and each 2D element is assigned a scalar value h_e that quantifies the local gap of the position occupied by that element, expressed as the averaged nodal gap value:

$$h_e = \frac{1}{3}\sum_{i=1}^{3} 2d_i \tag{1}$$

The geometric meaning of Eq. 1 is illustrated in Fig. 1 (a 2D medial axis representation is used for simplicity). Skeletons $\hat{\Omega}_1$ and $\hat{\Omega}_2$ are then linked through a set of 1D interface

elements, denoted as $\hat{\Omega}_3$, to restore the original connectivity. For each 1D element connecting the sets of triangular meshes, a cross-sectional area A_e is assigned, which is approximated as an average between the areas of all the triangles connected to the element (as illustrated in Fig. An example of geometry with labeled domains is shown in Fig. 2. All skeleton meshes presented in this work are generated numerically using the Voronoi method, starting from an input mesh created through Gmsh [34] or TexGen [35]. The open-source library QHull [36] is used to compute Voronoi diagrams from a set of input points. The input nodes used to generate the skeleton mesh are the ones belonging to the surfaces where a channel/yarn interface or a no-slip velocity condition occurs. Inlet and outlet regions do not participate in the generation of the skeleton mesh. This avoids the generation of spurious branches in the skeleton.

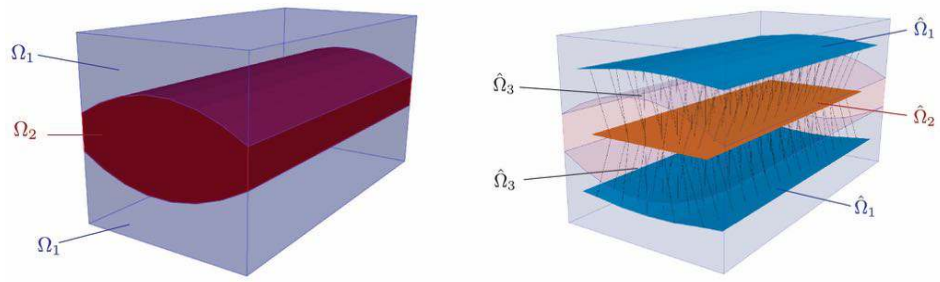

(a) Input geometry

(b) Dual-scale medial skeleton (hybrid skeleton mesh)

Figure 2: Yarn immersed in a channel: a) original three-dimensional geometry b) corresponding hybrid skeleton mesh

2.2. Dual Scale Skeleton model

In the input 3D domain, subdomains Ω_1 (channels) and Ω_2 (yarns) are continuous at the interface. At any point, for an incompressible fluid with constant density, the continuity equation is expressed as:

$$\nabla \cdot \boldsymbol{u} = f \tag{2}$$

where $\boldsymbol{u}$ is the three-dimensional velocity and f indicates a point-wise source term.

By assumption, introducing the test function v, Eq. 2 is transformed in its weak form to take advantage of the additive property of integrals:

$$\int_{\Omega} \nabla \cdot \boldsymbol{u}\ v\ d\boldsymbol{x} = \int_{\Omega} f\ v\ d\boldsymbol{x} \tag{3}$$

$$\int_{\Omega_1} \nabla \cdot \boldsymbol{u}\ v\ d\boldsymbol{x} + \int_{\Omega_2} \nabla \cdot \boldsymbol{u}\ v\ d\boldsymbol{x} = \int_{\Omega_1} f\ v\ d\boldsymbol{x} + \int_{\Omega_2} f\ v\ d\boldsymbol{x} \tag{4}$$

The terms in Eq. 4 can be isolated and treated separately based on separation of domains.

2.2.1. Channel domain

The terms in Eq. 4, defined in the channel domain Ω_1, are expressed as:

$$\int_{\Omega_1} \nabla \cdot \boldsymbol{u}\ v\ d\boldsymbol{x} = \int_{\Omega_1} f\ v\ d\boldsymbol{x} \tag{5}$$

To take advantage of the skeleton mesh, lubrication approximation is adopted in the channels, similarly to what was done in [37]. The three-dimensional domain Ω_1 is replaced by its two-dimensional skeleton $\hat{\Omega}_1$ by substituting the point-wise velocity field $\boldsymbol{u}$ with the gap-averaged velocity $\langle \boldsymbol{u} \rangle$. This operation is possible by applying the spatial averaging theorem of the divergence operator [38], which states:

$$\langle \nabla \cdot \boldsymbol{u} \rangle = \nabla \cdot \langle \boldsymbol{u} \rangle + q \tag{6}$$

where the term $q = \frac{1}{V} \int_{\Gamma_w} \boldsymbol{n}_{\perp} \cdot \boldsymbol{u}\, dx$ will be used to represent the fluid traveling across the interface and introduce the coupling between the two domains. By assumption, the Reynolds gap-averaged velocity related to the lubrication approximation is adopted. For creeping flow inside a gap of thickness h, the averaged velocity is expressed as:

$$\langle \boldsymbol{u} \rangle = \frac{h^2}{12\mu} \nabla p \tag{7}$$

Eq. 5 is expressed in its weak form over one single 2D element $\hat{\Omega}_e$ of the channel's skeleton mesh:

$$\underbrace{\int_{\hat{\Omega}_e} \frac{h_e}{\mu} \frac{h_e^2}{12} \nabla p \nabla v \, d\boldsymbol{x}}_{a.1} - \underbrace{\int_{\partial\hat{\Omega}_e} \frac{h_e}{\mu} g v \, dx}_{a.2} + \underbrace{\int_{\hat{\Omega}_e} h_e q v \, d\boldsymbol{x}}_{\text{b}} = \underbrace{\int_{\hat{\Omega}_e} h_e f v \, d\boldsymbol{x}}_{c} \tag{8}$$

where the terms in Eq. 8 refer to: a.1) internal element flux balance; a.2) Neumann flux boundary condition with $g = \frac{h^2}{12} \nabla p \cdot \boldsymbol{n}$ on element boundary $\partial\hat{\Omega}_e$; b) interface flux term; c) external source term. Test function $v = \eta_i$, and trial function $p = p_i \eta_i$ are adopted, where η_i designates linear shape functions. Following the classical theory of finite elements Eq. 8 is expressed in matrix-vector form:

$$\begin{bmatrix} \\ K_{\hat{\Omega}_1} \\ \\ \end{bmatrix} \begin{bmatrix} \\ p \\ \\ \end{bmatrix} + \begin{bmatrix} \\ q \\ \\ \end{bmatrix} = \begin{bmatrix} \\ b_{\hat{\Omega}_1} \\ \\ \end{bmatrix} \tag{9}$$

in which $[b_{\hat{\Omega}_1}]$ represents imposed fluxes (terms a.2 and c in Eq. 8), $[q]$ represents the volumetric flux flowing to another domain (term b in Eq. 8), and the local element stiffness matrix of the system is:

$$[K_e] = \left[\frac{1}{\mu} \int_{\hat{\Omega}_e} \frac{h_e^3}{12} \nabla \eta^T \nabla \eta \, d\boldsymbol{x} \right] \tag{10}$$

2.2.2. Yarn domain

The terms in Eq. 4 that apply to the yarn domain are:

$$\int_{\Omega_2} \nabla \cdot \boldsymbol{u} \; v \; d\boldsymbol{x} = \int_{\Omega_2} f \; v \; d\boldsymbol{x} \tag{11}$$

By the spatial averaging theorem on operators [38], the point-wise velocity in Eq. 11 is replaced by the corresponding volume-averaged velocity $\langle \boldsymbol{u} \rangle$, plus an interface term q, as done for the domain $\hat{\Omega}_1$. Following the same derivation, the same matrix-vector assembly form of Eq. 9 is obtained:

$$\begin{bmatrix} \\ K_{\hat{\Omega}_2} \\ \\ \end{bmatrix} \begin{bmatrix} \\ p \\ \\ \end{bmatrix} + \begin{bmatrix} \\ q \\ \\ \end{bmatrix} = \begin{bmatrix} \\ b_{\hat{\Omega}_2} \\ \\ \end{bmatrix} \tag{12}$$

Here, Darcy's law is adopted as the governing equation to describe the velocity in the domain $\hat{\Omega}_2$, expressed as:

$$\langle \boldsymbol{u} \rangle = \frac{K_{\parallel}}{\mu} \nabla p \tag{13}$$

where $K_{\parallel}$ is the longitudinal permeability assigned to the yarn. The transverse permeability of the yarn will be handled separately, by the interface elements $\hat{\Omega}_3$. The local element stiffness matrix of the system is now:

$$[K_e] = \left[\frac{1}{\mu} \int_{\hat{\Omega}_e} h_e K_{\parallel} \nabla \eta^T \nabla \eta \, d\boldsymbol{x} \right] \tag{14}$$

2.2.3. Interface domain

The subdomains $\hat{\Omega}_1$ and $\hat{\Omega}_2$ are interconnected by an array of 1D elements, labeled as $\hat{\Omega}_3$, representing the interface in between. These elements cannot be related to some physical space, but merely represent a connection between interacting nodes between which an exchange of fluid is allowed. Fig. 3 shows a typical interface element from $\hat{\Omega}_3$. The internal flux in the element can be expressed as:

$$q_{\text{int}} = (\boldsymbol{u} \cdot \boldsymbol{n}) A_e = u A_e \tag{15}$$

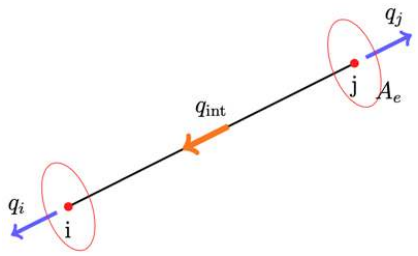

Figure 3: Interface element and the internal fluxes

where u is the axial velocity of the flux, in direction of the rod, and A_e is the cross-sectional area associated with the element. Local conservation of mass can be expressed as:

$$\begin{aligned} \text{node (i)} : \quad & q_i + q_{\text{int}} = 0 \\ \text{node (j)} : \quad & q_j - q_{\text{int}} = 0 \end{aligned} \tag{16}$$

To close the system, a definition of flux velocity u in the interface element is needed. In the hybrid skeleton representation, the element spans inside both the channel and the yarn domains, always sharing one node with $\hat{\Omega}_1$ and one node with $\hat{\Omega}_2$. A modeling choice is made: the flow velocity in the interface is modeled using Darcy's law in the portion of the element inside Ω_2, and $u = 0$ is assumed in the portion of the element inside Ω_1 (no transverse flow in the channel region to be consistent with the lubrication approximation). Darcy's velocity in the 1D element is expressed as:

$$u = -\frac{K_t}{\mu}\frac{\partial p}{\partial s} \tag{17}$$

where K_t is the yarn transverse permeability and s denotes the curvilinear coordinate of the 1D element. To be consistent with the assumptions made about the velocity, it is necessary to properly define the pressure derivative $\partial p/\partial s$ of Eq. 17 so that only the yarn region is taken into account. This can be achieved by assuming a linear pressure gradient:

$$\frac{\partial p}{\partial s} = \frac{p_i - p_j}{L_e\ \delta_e} \tag{18}$$

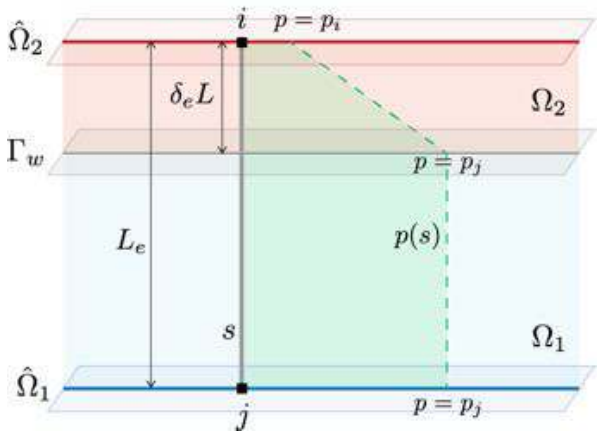

Figure 4: 1D interface element $\hat{\Omega}_3$ connecting the domains $\hat{\Omega}_1$, $\hat{\Omega}_2$. A linear pressure gradient is assumed in the yarn section of the element

where L_e is the total length of the element, and δ_e is a scalar coefficient corresponding to the fraction of the element length which is immersed in the yarn domain Ω_1 in the input geometry. A schematic representation of the pressure field as modeled on the interface elements is shown in Fig. 4. Adopting this expression, the linear system from Eq. 16 becomes:

$$\begin{aligned} q_i - \tfrac{K_t}{\mu}\tfrac{p_i - p_j}{L_e\,\delta_e} A_e = 0 \\ q_j + \tfrac{K_t}{\mu}\tfrac{p_i - p_j}{L_e\,\delta_e} A_e = 0 \end{aligned} \quad \rightarrow \quad \begin{vmatrix} q_i \\ q_j \end{vmatrix} = \begin{bmatrix} K_e \end{bmatrix} \begin{vmatrix} p_i \\ p_j \end{vmatrix} \tag{19}$$

with

$$[K_e] = \frac{K_t\, A_e}{\mu\, L_e\, \delta_e} \begin{bmatrix} 1 & -1 \\ -1 & 1 \end{bmatrix} \tag{20}$$

This system expresses the local net flux balance for a 1D interface element $\in \hat{\Omega}_3$ between nodes i and j. A global system of equations can be formulated by assembling

all $\hat{\Omega}_3$ elements, to create a system of nDOFs equations:

$$\begin{bmatrix} \\ q \\ \\ \end{bmatrix} = \begin{bmatrix} \\ K_{\hat{\Omega}_3} \\ \\ \end{bmatrix} \begin{bmatrix} \\ p \\ \\ \end{bmatrix} \tag{21}$$

2.2.4. Global assembly

Finally by assembling Eqs. 9, 12 and 21, a global form of nDOFs equations is obtained:

$$\begin{bmatrix} \\ K_{\hat{\Omega}} \\ \\ \end{bmatrix} \begin{bmatrix} \\ p \\ \\ \end{bmatrix} = \begin{bmatrix} \\ b \\ \\ \end{bmatrix} \tag{22}$$

where $[K_{\hat{\Omega}}] = [K_{\hat{\Omega}_1}]+[K_{\hat{\Omega}_2}]+[K_{\hat{\Omega}_3}]$ is a $n \times n$ global stiffness matrix, $[p]$ is the $n \times 1$ nodal values vector and $[b]$ is the $n \times 1$ right-hand side vector of Eq. 3, n being the number of DOFs. The system of equations in Eq. 22 can be solved for the nodal coefficients $[p]$ provided that some boundary conditions are prescribed.

2.3. Model validation

The DSS model is validated numerically by comparing it with a reference model. A Stokes-Brinkman (SB) solution computed on a full-dimensional domain is adopted as reference and compared with the DSS solution computed on the corresponding skeleton mesh. The numerical solution of the SB model is computed using the FEniCS finite element library [39, 40] by solving a mixed formulation problem composed of three equations, respectively Stokes equation on Ω_1, Darcy-Brinkman equation on Ω_2 and continuity equation on Ω_1, Ω_2:

$$\mu\nabla^2\boldsymbol{u} - \nabla p = \mathbf{0} \quad \text{on} \quad \Omega_1 \tag{23}$$

$$-\phi\nabla p + \mu\nabla^2\langle\boldsymbol{u}\rangle - \frac{\mu\,\phi}{K}\langle\boldsymbol{u}\rangle = 0 \quad \text{on} \quad \Omega_2 \tag{24}$$

$$\nabla\cdot\boldsymbol{u} = 0 \quad \text{on} \quad \Omega_1, \Omega_2 \tag{25}$$

For simplicity, a scalar permeability term K was adopted in Eq. 24, but this could be replaced by a tensorial term to reflect anisotropy in the porous domain. At the current level of development, this possibility has not been explored yet. The test geometry is composed of two layers: a channel domain Ω_1 on top, and a porous domain Ω_2 underneath it. The geometry is shown in Fig. 5 in which dimensions and boundaries are indicated. Boundary conditions of unitary pressure difference between inlet Γ_{in} and outlet Γ_{out} is imposed. For the solution of Brinkman's equation, material parameters $\phi = 0.3$, $\mu = 1$ Pa s and K = 1E-04 m^2 are used.

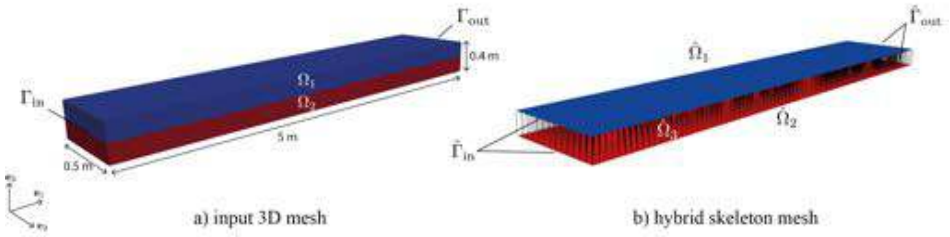

Figure 5: The geometry used for DSS model test and validation

The DSS model solution is computed using an in-house written Matlab solver. Solutions are computed on a machine equipped with an Intel Core i5-6500 CPU 3.20GHz and 16 GB of memory. To be coherent with the SB model, $K_{\|} = K_t = K$ are selected in the DSS formulation. Solutions fields of pressure and velocity are computed. Mesh parameters and solution values are provided in Table 1. The solutions of veloc-

Model	N_{elem}	CPU t [s]	$\overline{u}_{\Omega_1}$ [m/s]	$\overline{u}_{\Omega_2}$ [m/s]
SB (ref.)	63316	97	7.72E-04	2.00E-05
DSS	9354	0.04	6.75E-04	2.02E-05

Table 1: Results of dual-scale validation test case described in Fig. 5

ity field in the channel direction (u_1) are shown in Fig. 6 for both models. One can observe the typical velocity profile from Stokes-Brinkman model: the parabolic profile in the channel region and the plug flow profile in the porous region, connected by the characteristic boundary layer near the interface. To extract some values that can be compared with the DSS model, velocities from the SB solution are phase-averaged ($\overline{u}_{\Omega_1}$, $\overline{u}_{\Omega_2}$). A series of considerations can be drawn by examining the velocity results in

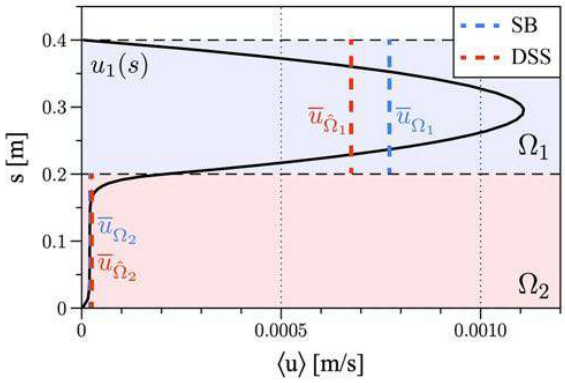

Figure 6: DSS model validation: velocity comparison between SB and DSS models

the two domains individually. In the channel domain (Ω_1), the DSS model yields a relative error of $\xi = 12.5\%$ from the reference value. This error arises due to the no-slip interface boundary condition adopted in the DSS model (Poiseuille velocity profile), while in the SB model an interface-slip velocity is present [41, 42, 43]. This results in an underestimation of the velocity field in the channel domain in the DSS model. In the porous domain (Ω_2), a much closer agreement between the velocity solutions is observed ($\xi = 1\%$). This suggests that away from the interface, when the Darcy velocity is stabilised, the DSS model agrees well with the SB model. The CPU time needed to compute solution according to the models is different. One must remark

that the number of elements is also different. Even so, the DSS model shows a large advantage in CPU time. In the light of the errors on velocity, the DSS model yields reasonable results, especially with regard to CPU time gains. However, this single test case should not be considered exhaustive for the quantification of the DSS model approximation: additional validations should be carried out over more complex domains in order to properly assess the potential and limitation of the model. In particular, a DSS/SB transient flow simulation would be valuable to assess the applicability of the model to filling simulations by comparing the evolution of velocities throughout the process. However, at the current state of development such validation was not carried out. In the remainder instead, transient flow simulations using the DSS model alone are presented.

2.4. Filling simulation

Representative test cases are presented in which a dual-scale filling simulation is carried out at the mesoscale using the DSS model. To do so, the FE/CV software LIMS was used [44]. The capability of LIMS to support mixed 2D and 1D element meshes has already allowed one to simulate the dual-scale impregnation of tows [45, 46]. The DSS model can be implemented in LIMS by assigning the material and process variables via the input file, so that the same form of equations as in section 2.2 are preserved. A detailed explanation of the implementation of the DSS model in LIMS can be found in [33]. For all cases, the procedure followed is: a 3D input textile geometry is generated, its hybrid skeleton mesh is created and the dual-scale filling is simulated using LIMS. Boundary conditions of inlet pressure ($p_{\text{in}} = 1.0E+03$ Pa on $\hat{\Gamma}_{\text{in}}$) and outlet pressure ($p_{\text{out}} = 0$ Pa on $\hat{\Gamma}_{\text{out}}$) are used. The inlet pressure value, not representative of real processing conditions, is chosen to avoid a too fast filling of the mesh, since the domain lengths are in the order of centimeters. All test cases were run on the same machine as indicated in Section 2.3. LIMS uses a direct solver on a single CPU core to solve the

pressure field at each time step.

Case	Description	N_{elem}	Memory	CPU t
A	Yarn immersed in channel	19456	33 MB	19 s
B a)	Yarns array - high yarn perm.	383273	0.99 GB	3323 s
B b)	Yarns array - low yarn perm.	383273	1.22 GB	3608 s
B c)	Yarns array - transversely isotropic yarn	383273	1.29 GB	4020 s
B d)	Yarns array - central racetrack	402404	1.11 GB	3748 s
C	Multi-layer - central racetrack	643323	1.56 GB	4280 s

Table 2: Dual scale filling test cases using DSS model: numerical solution values

2.4.1. Test case A

For this case, the input geometry used is the one studied in Section 2.2, shown in the figure 7a. The purpose is to demonstrate the dual-scale filling mechanism using the simplest scenario: one yarn immersed in an empty channel. The yarn is assigned an isotropic permeability value $K_{\parallel} = K_t = 1.0E - 11$ m^2. Boundary conditions are applied, the DSS filling is computed by LIMS and shown as a time sequence in Fig. 8. One can notice that the faster flow in the channels $\hat{\Omega}_1$ is ahead of the slower flow front

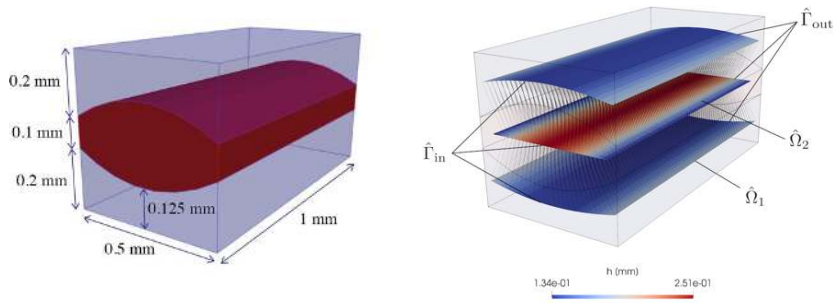

(a) Input geometry

(b) Hybrid skeleton mesh

Figure 7: Test case A: geometry

within the yarn $\hat{\Omega}_2$ and fills the channels before the yarn is fully impregnated. The role of the interface elements is evidenced by the partially-saturated region that is ahead of the saturated flow front in the yarn. This is the effect of the transverse flow coming into the yarn from the already filled channel regions above and below. One can also

notice the concave shape of the flow front in the yarn, which is due to the elliptical cross-section of the yarn with higher thickness in the middle (more volume to fill). The CPU cost needed to compute the dual-scale filling is of the order of seconds (Table 2).

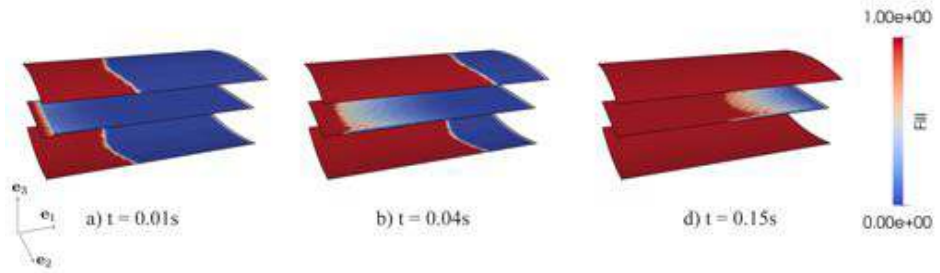

Figure 8: Test case A: result filling sequence

2.4.2. Test case B

The purpose of this test case is to study how the dual-scale filling of an array of yarns is affected by local features: in particular, the yarn permeability and the presence of racetracks. An array of four yarns are lined up in a channel defined by two parallel plates, as shown in Fig. 9a. The dimensions of gaps surrounding the yarns have been exaggerated on purpose to highlight the fluid transfer phenomenon from the resin channels to the yarns. In particular, thin channel slits are modeled above and below tows so that they may be filled with resin and trigger a transverse impregnation of the tow. These channels may not exist in a real material and their presence is not necessary for the model. Flow is prescribed in the direction along the yarns. Four different scenarios are considered: a) the yarns are assigned the same isotropic permeability value as in case A ($K_{\parallel} = K_t = 1.0E-11$ m^2); b) the yarns permeability is decreased by one order of magnitude ($K_{\parallel} = K_t = 1.0E-12$ m^2); c) a transversely isotropic permeability is assigned to the yarns, with a lower transverse permeability than in direction of the fibers ($K_{\parallel} = 1.0E-12$ m^2, $K_t = 1.0E-13$ m^2) ; d) a racetrack gap of size $d = 0.5$ mm is introduced in the middle of the array. For each

of these scenarios an input mesh is created, its hybrid skeleton mesh is extracted and the filling is simulated. The hybrid skeleton mesh from scenario a) is shown in Fig. 9b. The results from the four scenarios are displayed in Fig. 11 at an arbitrary simulation

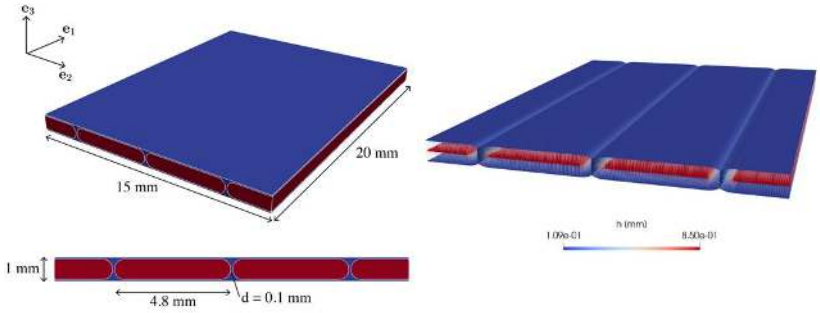

(a) Input geometry (b) Hybrid skeleton mesh

Figure 9: Test case B: Input geometry and hybrid skeleton mesh

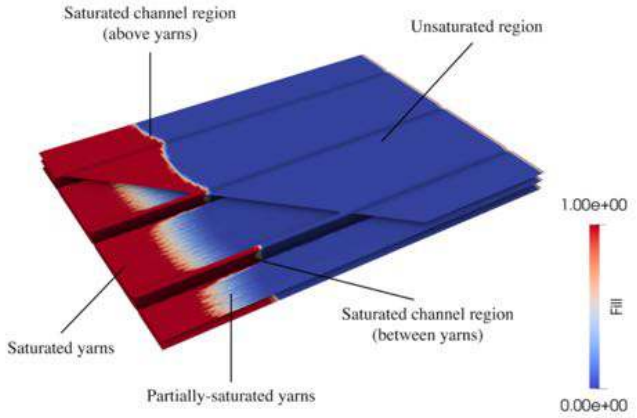

Figure 10: Test case B: close-up view of the solution features and visualisation cut of the inter-layers channel domain

time of $t = 16s$. For the visualisation of results, the top of the mesh has been hidden to show both channels and yarns underneath at the same time as illustrated in Fig. 10. In all scenarios, the flow front proceeds faster in the inter-yarn channels, and follows after some lag distance in the yarns. Upstream of the fully saturated flow front in the yarns is a partially-saturated region caused by the transverse flow from the filled channels. The variation of isolated parameters has an observable effect on the flow. In Scenario b), the yarn permeability, both longitudinal and transverse, is one order of magnitude lower

than in Scenario a). As a consequence, the resin advances more slowly in the yarns, the lag distance from the flow front in the channels is increased and the partially-saturated region is longer. In Scenario c) the lower transverse permeability assigned to the yarns limits the flow rate of resin coming from the channels. As a consequence, the filling of the yarns is mainly longitudinal, with a distinct separation between the saturated and partially-saturated regions. In Scenario d) the larger racetrack between the two central yarns has a trailing effect on the entire flow front pattern. As the central channel is filled first, the transverse impregnation of the yarns originates from the center. Thus the DSS model is able to capture these local flow anomalies. All simulations require a higher CPU time to carry out than case A because of higher number of elements used and larger domain (20 × 15 mm). Values are reported in Table 2.

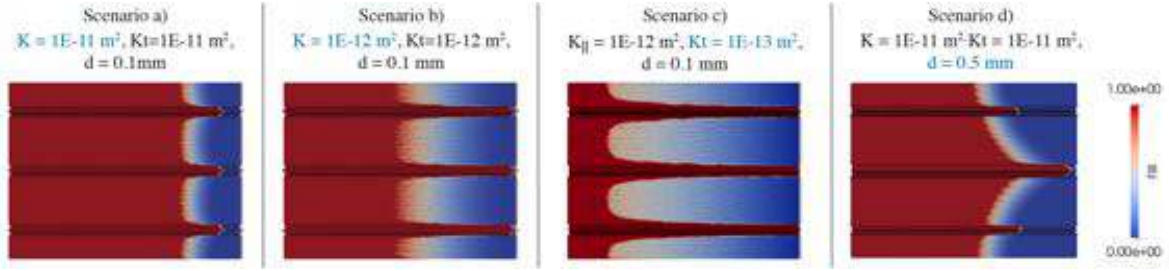

Figure 11: Test case B: result filling sequence

2.4.3. Test case C

In this test case the DSS model is used to simulate a more complex scenario: a four-layer quasi-UD layup with through-thickness interaction between layers. The layup follows the sequence of orientations (from the bottom): $\theta = [-45°, 0°, 45°, 0°]$. The domain has a size of 35 × 35 mm. As with the previous Test case B, the width of the fluid gaps between the tows has been exaggerated with respect to a real material. Thin gaps have been modeled between adjacent layers to allow some flow of resin between them and highlight the transverse impregnation of tows. However these inter-layer gaps do not typically exist within a preform in compacted state. The presence of these gaps

is not necessary for the model and a more realistic geometry with locally touching tows could equally be used. Furthermore, one single central racetrack is designed in the middle of the second layer in the stack. This local feature was included to add further complexity to the domain. The input geometry is shown in Fig. 12a. The hybrid

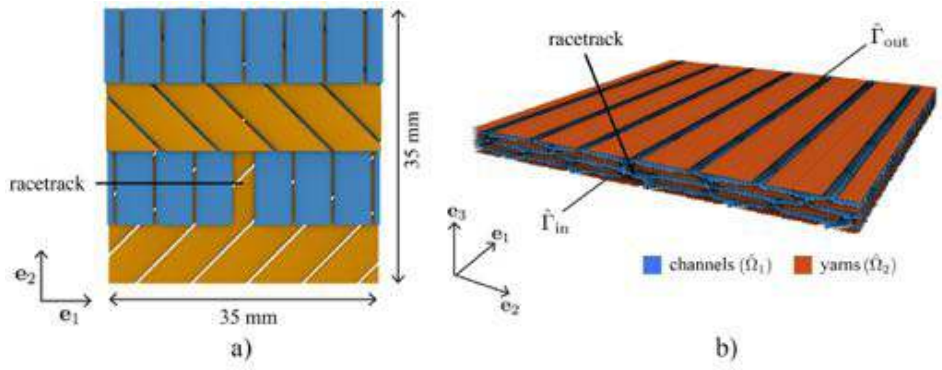

Figure 12: Test case C: a) input geometry and b) hybrid skeleton mesh

skeleton mesh is extracted and shown in Fig. 12b, where inlet and outlet regions are also indicated. The two main components of the hybrid skeleton, the channel domain mesh $\hat{\Omega}_1$ and the yarn domain mesh $\hat{\Omega}_2$, have been isolated in the figure. The flow front patterns in each layer are displayed in sequence in Fig. 13. For each layer, it is possible to see the yarns being progressively filled with the flow front preceded by the usual partially-saturated region as a result from the transverse infiltration. As expected the flow front in the channels is more advanced. The effect of the racetrack on the flow front can be observed in layer 2. Its influence can be observed also in the adjacent layers 1 and 3, less in layer 4 (the most distant). In particular, a yarn region which is located just above the racetrack is highlighted in layer 3: this unfilled yarn area is entrapped between the advancing flow front saturating the yarn and the transverse flow infiltrating from the racetrack. Such a flow pattern represents a potential risk of air entrapment and dry spot formation. CPU time with respect to number of elements is reported in Table 2.

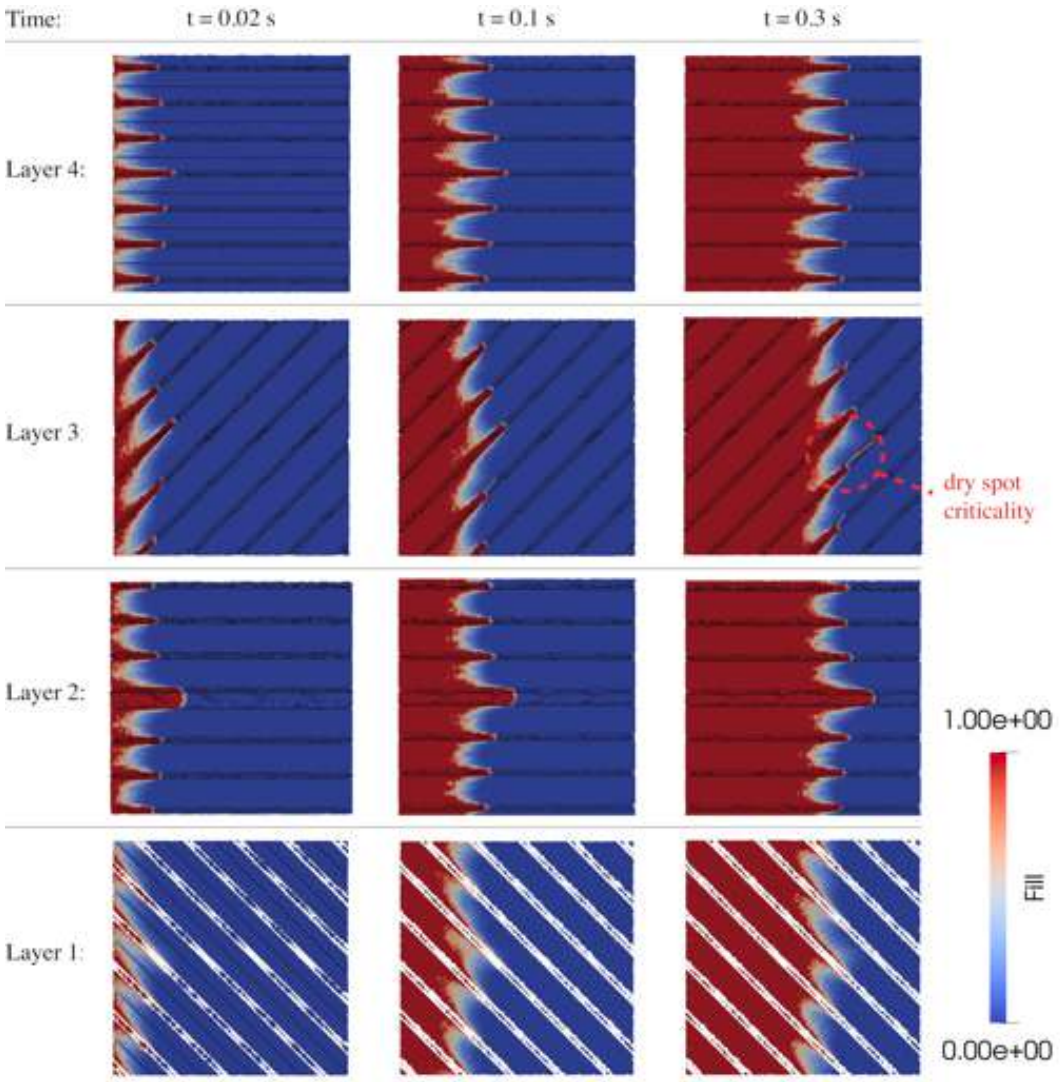

Figure 13: Test case C: result fill sequence

3. Conclusions

A new model was proposed which can handle the dual-scale flow onto a novel hybrid skeleton mesh. The accuracy of the DSS model was assessed by comparison against a full-dimensional Stokes-Brinkman solution, showing a maximum error of less than 15%. The model was implemented in a commercial software to simulate the dual-scale filling of dry textiles. A series of test cases were presented in which the filling of increasingly complex dual-scale porous domains was carried out on their hybrid

skeleton representation, at the benefit of the computational cost. At the current level of development, these test cases require further validation, which could be achieved only by either experimental measurement or by numerical comparison with reference solutions to assess the expected gain in computational time. It is worth to note that experimental validation is still very challenging because the dual scale flow in fabrics is difficult to monitor and subjected to experimental errors. Similarly, solving the same test cases numerically using a 3D Stokes-Brinkman transient flow solver on domains as large as the cases presented is a challenge pertaining to high-performance computation, which is out of scope. For these reasons, a rigorous validation of the DSS model has still to be improved and will be subject of future works. However, the results in all test cases show good qualitative agreement with how the flow is expected to behave in presence of their distinctive features (racetracks, low/high yarn permeability...). The approximations introduced by the DSS model are well balanced by the computational efficiency: filling simulations for all test cases were carried out in a CPU time of about one to two hours, over larger domains than typical RVEs. However, at the current state of development, only the SB/DSS validation case in Section 2.3 can provide some quantification of the computational savings that can be expected using this model, for a single time step (fully saturated flow). It is reasonable to believe that the same difference would apply when executing a transient flow simulation, where the problem of solving for pressure/velocity must be repeated at each time step, as in test cases A, B and C. However, at the moment, this still needs to be proven through further work.

The model proposed demonstrates potential for simulating the dual-scale filling of a textile directly at the mesoscale, taking into account any local features modeled in the input geometry. At the current state of development, the size of domains simulated is larger than typical RVEs but still far from the size of real parts. Therefore, the DSS model cannot be considered a replacement of macroscale Darcy models yet.

Future works will likely explore alternative methods to generate larger skeleton meshes efficiently, thus opening the way to simulate the filling of larger and larger parts using the DSS model.

Acknowledgements

This research was partially funded by Conseil Regional Pays de la Loire (grant number TEU29).

References

[1] S. G. Advani and E. M. Sozer, *Process modeling in composites manufacturing*, vol. 59. CRC Press, 2002.

[2] V. Michaud, "A review of non-saturated resin flow in liquid composite moulding processes," *Transport in porous media*, vol. 115, no. 3, pp. 581–601, 2016.

[3] B. Liu, S. Bickerton, and S. G. Advani, "Modelling and simulation of resin transfer moulding (rtm)—gate control, venting and dry spot prediction," *Composites Part A: applied science and manufacturing*, vol. 27, no. 2, pp. 135–141, 1996.

[4] S. Bickerton, H. C. Stadtfeld, K. V. Steiner, and S. G. Advani, "Design and application of actively controlled injection schemes for resin-transfer molding," *Composites Science and Technology*, vol. 61, no. 11, pp. 1625–1637, 2001.

[5] E. M. Sozer, S. Bickerton, and S. G. Advani, "On-line strategic control of liquid composite mould filling process," *Composites Part A: Applied Science and Manufacturing*, vol. 31, no. 12, pp. 1383–1394, 2000.

[6] R. S. Parnas, J. G. Howard, T. L. Luce, and S. G. Advani, "Permeability characterization. part 1: A proposed standard reference fabric for permeability," *Polymer composites*, vol. 16, no. 6, pp. 429–445, 1995.

[7] N. Kuentzer, P. Simacek, S. G. Advani, and S. Walsh, "Permeability characterization of dual scale fibrous porous media," *Composites Part A: Applied Science and Manufacturing*, vol. 37, no. 11, pp. 2057–2068, 2006.

[8] P. B. Nedanov and S. G. Advani, "Numerical computation of the fiber preform permeability tensor by the homogenization method," *Polymer composites*, vol. 23, no. 5, pp. 758–770, 2002.

[9] B. Verleye, R. Croce, M. Griebel, M. Klitz, S. V. Lomov, G. Morren, H. Sol, I. Verpoest, and D. Roose, "Permeability of textile reinforcements: Simulation, influence of shear and validation," *Composites science and technology*, vol. 68, no. 13, pp. 2804–2810, 2008.

[10] W. R. Hwang and S. G. Advani, "Numerical simulations of stokes–brinkman equations for permeability prediction of dual scale fibrous porous media," *Physics of Fluids*, vol. 22, no. 11, p. 113101, 2010.

[11] C. Wong, A. Long, M. Sherburn, F. Robitaille, P. Harrison, and C. Rudd, "Comparisons of novel and efficient approaches for permeability prediction based on the fabric architecture," *Composites Part A: Applied Science and Manufacturing*, vol. 37, no. 6, pp. 847–857, 2006.

[12] F. Desplentere, S. V. Lomov, D. Woerdeman, I. Verpoest, M. Wevers, and A. Bogdanovich, "Micro-ct characterization of variability in 3d textile architecture," *Composites Science and Technology*, vol. 65, no. 13, pp. 1920–1930, 2005.

[13] A. Gokce, K.-T. Hsiao, and S. G. Advani, "Branch and bound search to optimize injection gate locations in liquid composite molding processes," *Composites Part A: Applied Science and Manufacturing*, vol. 33, no. 9, pp. 1263–1272, 2002.

[14] J.-F. Delerue, S. V. Lomov, R. Parnas, I. Verpoest, and M. Wevers, "Pore network modeling of permeability for textile reinforcements," *Polymer composites*, vol. 24, no. 3, pp. 344–357, 2003.

[15] E. B. Belov, S. V. Lomov, I. Verpoest, T. Peters, D. Roose, R. Parnas, K. Hoes, and H. Sol, "Modelling of permeability of textile reinforcements: lattice boltzmann method," *Composites Science and Technology*, vol. 64, no. 7-8, pp. 1069–1080, 2004.

[16] H. Blum *et al.*, *A transformation for extracting new descriptors of shape*, vol. 43. MIT press Cambridge, MA, 1967.

[17] N. Amenta, S. Choi, and R. K. Kolluri, "The power crust, unions of balls, and the medial axis transform," *Computational Geometry*, vol. 19, no. 2, pp. 127–153, 2001. Combinatorial Curves and Surfaces.

[18] E. C. Sherbrooke, N. M. Patrikalakis, and E. Brisson, "An algorithm for the medial axis transform of 3d polyhedral solids," *IEEE transactions on visualization and computer graphics*, vol. 2, no. 1, pp. 44–61, 1996.

[19] Y. Tsao and K. S. Fu, "A parallel thinning algorithm for 3-d pictures," *Computer graphics and image processing*, vol. 17, no. 4, pp. 315–331, 1981.

[20] D. Morgenthaler, "Three-dimensional simple points: serial erosion, parallel thinning, and skeletonization. tr–1005," *Computer Science Center, University of Maryland, College Park, MD*, vol. 20742, 1981.

[21] Z. Jiang, M. I. J. Van Dijke, S. Geiger, J. Ma, G. D. Couples, and X. Li, "Pore network extraction for fractured porous media," *Advances in Water Resources*, vol. 107, pp. 280–289, 2017.

[22] G. Borgefors, "On digital distance transforms in three dimensions," *Computer vision and image understanding*, vol. 64, no. 3, pp. 368–376, 1996.

[23] P. K. Saha, G. Borgefors, and G. S. di Baja, "A survey on skeletonization algorithms and their applications," *Pattern recognition letters*, vol. 76, pp. 3–12, 2016.

[24] O. Reynolds, "Iv. on the theory of lubrication and its application to mr. beauchamp tower's experiments, including an experimental determination of the viscosity of olive oil," *Philosophical transactions of the Royal Society of London*, no. 177, pp. 157–234, 1886.

[25] D. Dowson, "A generalized reynolds equation for fluid-film lubrication," *International Journal of Mechanical Sciences*, vol. 4, no. 2, pp. 159–170, 1962.

[26] R. Zimmerman, S. Kumar, and G. Bodvarsson, "Lubrication theory analysis of the permeability of rough-walled fractures," *International journal of rock mechanics and mining sciences & geomechanics abstracts*, vol. 28, no. 4, pp. 325–331, 1991.

[27] P. Ranjith and D. Viete, "Applicability of the 'cubic law'for non-darcian fracture flow," *Journal of Petroleum Science and Engineering*, vol. 78, no. 2, pp. 321–327, 2011.

[28] M. A. Dippenaar and J. L. Van Rooy, "On the cubic law and variably saturated flow through discrete open rough-walled discontinuities," *International Journal of Rock Mechanics and Mining Sciences*, vol. 89, pp. 200–211, 2016.

[29] M. S. Riasi, N. K. Palakurthi, C. Montemagno, and L. Yeghiazarian, "A feasibility study of the pore topology method (ptm), a medial surface-based approach to multi-phase flow simulation in porous media," *Transport in Porous Media*, vol. 115, no. 3, pp. 519–539, 2016.

[30] X. Li, Z. Jiang, J. Ma, and X. Wang, "A pore-skeleton-based method for calculating permeability and capillary pressure," *Transport in Porous Media*, vol. 124, no. 3, pp. 767–786, 2018.

[31] Z. Jiang, R. van Dijke, S. Geiger, G. Couples, and R. Wood, "Extraction of fractures from 3d rock images and network modelling of multi-phase flow in fracture-pore systems," in *International Symposium of the Society of Core Analysts, Aberdeen, Scotland*, Citeseer, 2012.

[32] F. Xiao and X. Yin, "Geometry models of porous media based on voronoi tessellations and their porosity–permeability relations," *Computers & Mathematics with Applications*, vol. 72, no. 2, pp. 328–348, 2016.

[33] S. Bancora, *Characterization of fabric layups by pressure print analysis and simulation of dual-scale flow based on topological skeletonization: application to composite materials processing*. PhD thesis, École Centrale Nantes, 2021.

[34] C. Geuzaine and J.-F. Remacle, "Gmsh: A 3-d finite element mesh generator with built-in pre-and post-processing facilities," *International journal for numerical methods in engineering*, vol. 79, no. 11, pp. 1309–1331, 2009.

[35] M. Sherburn, *Geometric and mechanical modelling of textiles*. PhD thesis, University of Nottingham, 2007.

[36] C. B. Barber, D. P. Dobkin, and H. Huhdanpaa, "The quickhull algorithm for convex hulls," *ACM TRANSACTIONS ON MATHEMATICAL SOFTWARE*, vol. 22, no. 4, pp. 469–483, 1996.

[37] W. L. Li and H. M. Chu, "Modified reynolds equation for coupled stress fluids–a porous media model," *Acta Mechanica*, vol. 171, no. 3, pp. 189–202, 2004.

[38] K. M. Pillai, "Governing equations for unsaturated flow through woven fiber mats. part 1. isothermal flows," *Composites Part A: Applied Science and Manufacturing*, vol. 33, no. 7, pp. 1007–1019, 2002.

[39] M. Alnæs, J. Blechta, J. Hake, A. Johansson, B. Kehlet, A. Logg, C. Richardson, J. Ring, M. E. Rognes, and G. N. Wells, "The fenics project version 1.5," *Archive of Numerical Software*, vol. 3, no. 100, 2015.

[40] A. Logg, K.-A. Mardal, and G. Wells, *Automated solution of differential equations by the finite element method: The FEniCS book*, vol. 84. Springer Science & Business Media, 2012.

[41] P. G. Saffman, "On the boundary condition at the surface of a porous medium," *Studies in applied mathematics*, vol. 50, no. 2, pp. 93–101, 1971.

[42] A. Mikelic and W. Jäger, "On the interface boundary condition of beavers, joseph, and saffman," *SIAM Journal on Applied Mathematics*, vol. 60, no. 4, pp. 1111–1127, 2000.

[43] Y. Cao, M. Gunzburger, F. Hua, and X. Wang, "Coupled stokes-darcy model with beavers-joseph interface boundary condition," *Communications in Mathematical Sciences*, vol. 8, no. 1, pp. 1–25, 2010.

[44] P. Simacek and S. G. Advani, "Desirable features in mold filling simulations for liquid composite molding processes," *Polymer Composites*, vol. 25, no. 4, pp. 355–367, 2004.

[45] P. Simacek and S. G. Advani, "A numerical model to predict fiber tow saturation during liquid composite molding," *Composites science and technology*, vol. 63, no. 12, pp. 1725–1736, 2003.

[46] S. Facciotto, P. Simacek, S. G. Advani, and P. Middendorf, "Modeling of anisotropic dual scale flow in rtm using the finite elements method," *Composites Part B: Engineering*, vol. 214, p. 108735, 2021.